Volume 13 | Number 3 | 3 February 2026

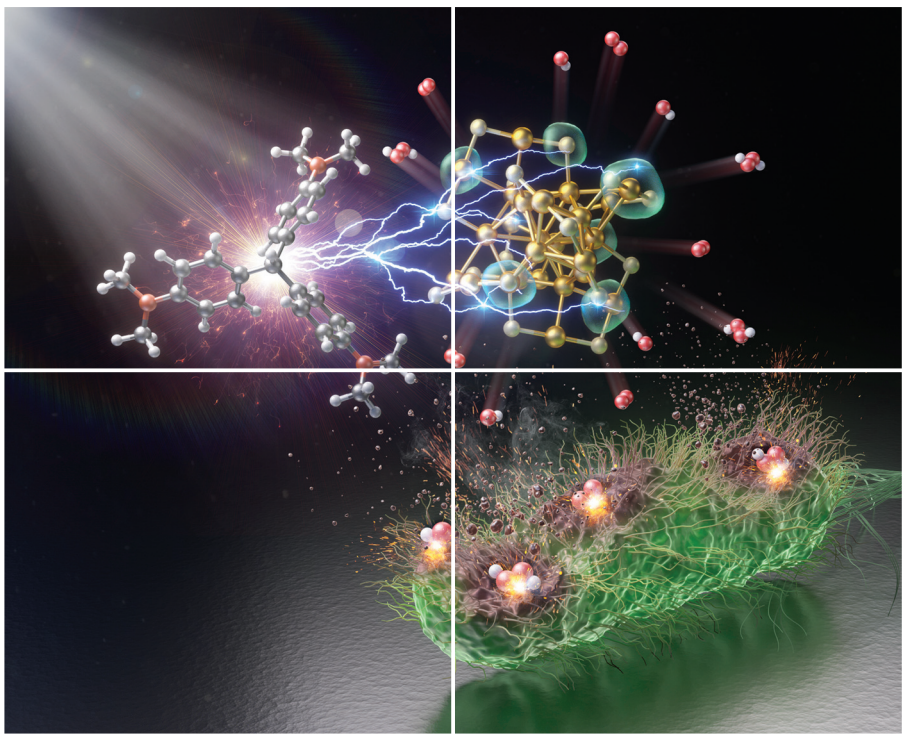

INORGANIC CHEMISTRY

FRONTIERS

CCS 中国化学会 CHINESE CHEMICAL SOCIETY
PEKING UNIVERSITY 1898
ROYAL SOCIETY OF CHEMISTRY
rsc.li/frontiers-inorganic

INORGANIC CHEMISTRY FRONTIERS

RESEARCH ARTICLE

View Article Online
View Journal | View Issue

Cite this: *Inorg. Chem. Front.*, 2026, **13**, 941

A 3D-printed pre-filter with a crystal violet–gold nanocluster hybrid for a reusable visible-light-activated antimicrobial air filtration system

Jae Hak Shin,†[a] So Yeong Kim,†[b] Hyun Sung Kang,[b] In Ho Kim,[a] Joon Young Park,[a] Ki Joon Heo,*[b] Gi Byoung Hwang*[c,d] and Jae Hee Jung*[a,e]

Received 1st October 2025,
Accepted 16th November 2025

DOI: 10.1039/d5qi02008e

rsc.li/frontiers-inorganic

Airborne microorganisms pose a persistent threat to public health. In this study, we present a reusable, visible-light-activated antimicrobial filtration system that combines a crystal violet–gold nanocluster (Au@CV)-coated pre-filter with a conventional dust-capturing main filter. Under visible-light irradiation, the Au@CV pre-filter generates reactive oxygen species (ROS), enabling dual antimicrobial mechanisms: (i) direct inactivation of microbes deposited on the pre-filter surface and (ii) airflow-assisted ROS inactivation of microorganisms captured on the downstream main filter. The study of photobactericidal mechanisms shows that Au nanoclusters on CV promote charge-carrier transfer and redox reactions, leading to the generation of multiple ROS. The Au@CV filter achieved up to a 4.7-log reduction in viable bacteria after 3 h of exposure to visible light. Furthermore, ROS transported from the pre-filter to the main filter enabled ~98% antibacterial efficiency even in the absence of airflow, while the performance strongly depended on airflow direction and velocity, underscoring the critical role of airflow in ROS delivery. Additionally, the Au@CV filter remained stable after the tape adhesion test and water immersion. We believe that this work can open a new avenue for designing and realising practical antimicrobial technology against the threat of infectious bioaerosols.

1. Introduction

Airborne microorganisms, commonly referred to as bioaerosols, pose a significant threat to public health. They can penetrate the human respiratory system and cause severe infections,[1,2] making bioaerosols a major global health concern.[3] Among the available strategies to control airborne microorganisms, air filtration technology is the most widely employed. However, bioaerosols captured on filters may remain viable and can be released back into the air during filter replacement or disposal, posing a risk of secondary contamination.

To address this issue, various antimicrobial air filtration technologies have been suggested. Notably, strategies such as the fabrication of nature-inspired nano/microstructural patterns on filter fibres to induce mechano-bactericidal activity[4,5] or the deposition of photocatalytic materials that generate reactive oxygen species (ROS) under visible light have demonstrated substantial antimicrobial effects.[6–9] Recently, strategies combining mechano- and photobactericidal functions have been proposed. Park *et al.* (2025) introduced nanoblade-based surfaces functionalised with Rose Bengal, which simultaneously exerted mechanical damage to bacterial membranes and photodynamically generated ROS under visible light, achieving rapid inactivation of both *Escherichia coli* and *Staphylococcus aureus*.[10] Similarly, Kim *et al.* (2024) introduced peptide-conjugated puncturable nanostructures that integrate the mechano-bactericidal effect of sharp nanostructures with the chemical antimicrobial action of the LL-37 peptide.[11] This chemo–mechano synergistic strategy significantly enhanced both the capture and contact bactericidal effects of bioaerosols, achieving a 97.7% reduction in *E. coli* compared with bare filters. Moreover, active thermal sterilisation has also been proposed.[12] Han *et al.* (2022) demonstrated a copper nanowire-based air filter capable of thermally denaturing bacterial cells, which obtained 99.3% inactivation of *Geobacter anodireducens* within 10 min.[13]

Despite these advances, such technologies are strongly influenced by dust accumulation.[14] As dust deposits on the filter surface, the antimicrobial layer loses direct contact with

[a]*Department of Mechanical Engineering, Sejong University, Seoul 05006, Republic of Korea. E-mail: jaehee@sejong.ac.kr*
[b]*School of Mechanical Engineering, Chonnam National University, Gwangju 61186, Republic of Korea. E-mail: k.heo@jnu.ac.kr*
[c]*Department of Chemistry, University College London, London, WC1H 0AJ, UK. E-mail: gi-byoung.hwang.14@ucl.ac.uk*
[d]*Lab.M.0, Seoul 04799, Republic of Korea*
[e]*Department of Aerospace System Engineering, Sejong University, Seoul 05006, Republic of Korea*
†These authors contributed equally to this work.

microbes, while organic components of dust, such as pollen and plant debris, can provide a favourable environment for microbial growth by supplying nutrients,[15,16] resulting in a significant reduction in antimicrobial efficacy. This underscores the urgent need for next-generation air filters capable of maintaining antimicrobial activity regardless of dust accumulation.

In this study, we introduce a novel antimicrobial filtration system comprising a pre-filter that provides non-contact antimicrobial action and a downstream unit for dust collection. Conventional non-contact approaches, such as ultraviolet (UV) irradiation, ozone, or hydrogen peroxide application, typically require additional devices and energy sources.[17–19] In contrast, our system employs a pre-filter coated with gold nanocluster–crystal violet (Au@CV), which utilises visible light, a substantial portion of sunlight or indoor lighting to generate ROS. These ROS are subsequently transported downstream with the airflow to the main filter, ensuring sustainable antimicrobial activity even when the primary filtration layer is loaded with dust. For this strategy, the pre-filter should maintain high air permeability without functioning as a particulate-capturing layer. Electrospun nanofibre filters, which are widely used in high-efficiency filtration, can lead to reduced antimicrobial performance due to dust accumulation.[20–22] To address this issue, we employed 3D printing to precisely control the fibre diameter and pore geometry, enabling the fabrication of an open-mesh structure that minimises particulate deposition while maintaining high permeability.[23] To validate this concept, airborne *S. epidermidis* were captured on the filter system, and antibacterial performance was evaluated in an irradiation chamber under varying airflow conditions. The results demonstrated that the ROS generated at the pre-filter were successfully carried to the main filter, where they exhibited antibacterial activity. This approach provides a promising pathway for the development of next-generation antimicrobial air filters, offering safe and sustainable indoor air quality management.

2. Materials and methods

Fabrication of the thermoplastic polyurethane (TPU) pre-filter

TPU pre-filters were fabricated using a fused filament fabrication (FFF)-based three-dimensional (3D) printer (3DP-210F, Cubicon, Korea) equipped with a 0.4 mm nozzle. In accordance with the manufacturer's recommendations, a transparent TPU filament (Cubicon) with a diameter of 1.75 mm was extruded at a nozzle temperature of 230 °C and a bed temperature of 65 °C. The pre-filter geometry was designed as a mesh structure with a fibre diameter of 0.42 mm, a fibre-to-fibre spacing of 0.88 mm, and a total thickness of 1 mm. Under these conditions, a single disk-shaped pre-filter with a diameter of 1.27 cm (0.5 inches) was fabricated within approximately 90 s. A detailed computer-aided design (CAD) schematic of the pre-filter, along with the corresponding scanning electron microscopy (SEM) image, is provided in the SI (Fig. S1). The TPU pre-filter morphology was examined using an optical microscope (BX53M, Olympus, Japan). The mean fibre diameter was determined by measuring more than 100 individual fibres using JENOPTIK GRYPHAX software (Jenoptik AG, Jena, Germany).

Synthesis of gold nanoclusters (AuNCs)

For the synthesis of L-cysteine-protected AuNCs ($[Au_{25}(Cys)_{18}]$), 40 mg of tetrachloroauric acid and 18 mg of L-cysteine were added to deionised (DI) water (93.5 mL) under vigorous stirring. The pH of the solution was adjusted to 11.85 by adding NaOH.[24] The reaction vessel was then saturated with 0.1 MPa CO for 1 min. The mixture was sealed and allowed to react under gentle stirring (500 rpm) at room temperature for 45 min before being heated to 70 °C.

Characterisation of AuNCs

The composition of the synthesised AuNCs was determined by dissolving the dried cluster powder in DI water, and then the solution was infused into an electrospray ionisation-mass spectrometer (ESI-MS, XEVO G2-XS Qtof, Waters Co., USA) at a flow rate of 100 μL min^{-1}. The electrospray ionisation (ESI) was operated in negative mode, and heated nitrogen (the desolvation gas) was supplied into the spectrometer at a flow rate of 800 L h^{-1}. The negatively charged ions were analysed using a mass spectrometer (MS). UV-Vis absorption spectra of AuNC solutions were measured at 300–800 nm using a UV-Vis-NIR spectrophotometer (UV-3600i Plus, Shimadzu, Japan). The size and morphology of AuNCs were examined by high-resolution transmission electron microscopy (HRTEM; Titan G2 Cube 60–300, FEI, USA). For HRTEM analysis, a droplet of diluted AuNC solution was placed onto a TEM grid, air-dried, and imaged at an accelerating voltage of 80 kV.

Preparation of the Au@CV-coated pre-filter (Au@CV filter)

Crystal violet (CV, Sigma-Aldrich) was dissolved at 800 ppm in a mixture of acetone (100 mL), AuNCs (20 mL), and DI water (80 mL), or in a 1 : 1 mixture of acetone and DI water (100 mL each). A TPU pre-filter was immersed in this solution for 24 h. The coated filter was collected from the solution, rinsed twice with DI water to remove residual materials, and air-dried for 24 h in the dark. Filters containing only AuNCs were prepared using the same procedure without the addition of CV.

Characterisation of the pre-filter surface

The surface of the Au@CV filter was characterised by X-ray photoelectron spectroscopy (XPS; K-ALPHA$^+$, Thermo Fisher Scientific, USA) using an Al Kα source (h_ν = 1486.6 eV). Survey and high-resolution spectra of CV, Au, and the Au@CV filter were acquired under ultra-high vacuum (5.0×10^{-9} mbar). The binding energy scale was calibrated to the C 1s peak of adventitious carbon at 285.8 eV.

Antibacterial test

The antibacterial activity of the filters was assessed against *S. epidermidis* (KCTC 1917) and *E. coli* (KCTC 1039) under visible light and dark conditions. One of the bacterial colonies

grown on nutrient agar (Becton Dickinson, USA) was inoculated into nutrient broth (Becton Dickinson) and incubated at 37 °C with shaking at 200 rpm for 18 h. The cells were harvested by centrifugation (4000*g*, 15 min), washed with phosphate-buffered saline (PBS; 10 mL), and resuspended in PBS to ~10^8 colony-forming units (CFU) per mL. Aliquots (50 μL) of the bacterial suspension were deposited onto filters placed in colourless Petri dishes. Samples were exposed either to an LED lamp (LVG95S, 12 W; 400–800 nm; Osram, Germany) at a distance of 50–100 mm (5.8–11.9 mW cm^{-2}), to room light (0.04 mW cm^{-2}) or maintained in darkness. Following exposure, the filters were vortexed in 5 mL PBS for 1 min to extract viable bacteria from the filters. Serial dilutions were plated on nutrient agar and incubated at 37 °C for 24 h before colony enumeration. Each experiment was repeated three times.

Analysis of the key ROS contributing to antimicrobial activity

To identify the ROS responsible for the antibacterial activity of the Au@CV pre-filter, scavenger and quencher assays were performed. Scavengers and quenchers of ROS, including superoxide dismutase, catalase, mannitol, and L-histidine, were purchased from Sigma-Aldrich. *S. epidermidis* suspensions (~3.3×10^6 CFU mL^{-1}) containing individual ROS scavengers were prepared using the following: superoxide dismutase (~20 units mL^{-1}) for superoxide radicals ($O_2^{\bullet-}$), catalase (6–14 units mL^{-1}) for hydrogen peroxide (H_2O_2), mannitol (82 mM) for hydroxyl radicals ($^{\bullet}OH$), and L-histidine (2 mM) for singlet oxygen ($^1O_2$). Each Au@CV pre-filter sample was immersed in the bacterial suspension containing one type of scavenger and light irradiated for 3 h (11.9 mW cm^{-2}). The resulting suspension was serially diluted, and 100 μL was inoculated onto nutrient agar and incubated at 37 °C for 24 h. The number of bacterial colonies grown on the agar was then counted.

Steady-state and time-resolved photoluminescence (PL) spectroscopy

Steady-state PL spectra of CV and the Au@CV filter (2.0 cm × 2.0 cm) were measured at wavelengths of 600–780 nm using a photospectrometer (FluoroLog-QM, Horiba Scientific, Japan) with 560 nm excitation. PL lifetimes were measured using the same system equipped with time-correlated single-photon counting. Pulsed excitation at 560 nm (100 MHz repetition rate, <140 ps pulse width) was provided by a diode laser (DeltaDiode, Horiba Scientific, Japan), and fluorescence was monitored at 620 nm over time scales up to 100 ns (resolution ~26.7 ps). Decay curves were normalised to the maximum PL intensity to evaluate lifetime changes upon Au loading.

Band alignment determination

XPS was used to determine the band offsets of CV and AuNCs. The energy difference between the N 1s core level (CL) and the highest occupied molecular orbital (HOMO) band maximum (HBM) was measured for each material. The relative CL shift between CV and AuNCs was then calculated, and band alignment was obtained according to eqn (1):[25]

$$\Delta E_{HBM} = (E_{CL}^{AuNC} - E_{HBM}^{AuNC}) - (E_{CL}^{CV} - E_{HBM}^{CV}) - \Delta E_{CL} \quad (1)$$

where E_{CL}^{AuNC} and E_{CL}^{CV} are the N 1s CL energies of AuNCs and CV, respectively. E_{HBM}^{AuNC} and E_{HBM}^{CV} are the HBM energies of AuNCs and CV, respectively. ΔE_{CL} is $E_{CL}^{AuNC} - E_{CL}^{CV}$.

Filtration performance evaluation

A suspension of *S. epidermidis* was aerosolised using a six-jet Collison nebuliser (CH Technologies, USA) with clean air injected at a flow rate of 5 L min^{-1}, and excess moisture was removed using a diffusion dryer (Fig. S2). The particle size distribution and concentration of bacterial aerosols were monitored with an optical particle counter (OPC; 11-D, GRIMM Aerosol Technik, Germany). Filtration efficiency (η) was calculated using eqn (2):

$$\eta = 1 - C_{outlet}/C_{inlet} \quad (2)$$

where C_{inlet} and C_{outlet} represent the particle $cm^{-3}{}_{air}$ number concentration (particle cm^{-3} air) of bacterial aerosols at the filter holder inlet and outlet, respectively. The pressure drops across the filter (ΔP) were measured using a digital manometer (Testo 400, TESTO Inc., Germany).

Airflow-assisted antibacterial testing

Airflow-assisted antibacterial activity of the Au@CV filter was evaluated in a custom-designed irradiation chamber (Fig. S3). The chamber was equipped with an LED light source, a humidifier, an air circulation fan, and a filter holder positioned beneath the light source. Constant airflow across the filter surface was maintained using a pump with a ball valve. Bacterial aerosols were introduced for 5 min onto each test filter. After the aerosol deposition, filters were irradiated with visible light for 2 h. The Au@CV filter and the main filter were separated and analysed using CFU assays.

3. Results and discussion

Fabrication and characterisation of 3D-printed pre-filters

Our system is designed to decouple the functions of physical removal and photochemical microbial inactivation. The downstream main filter is dedicated solely for particle capture, whereas the Au@CV pre-filter acts as a reactive source of ROS that are transported downstream with airflow. This functional separation allows the main filter to retain its intrinsic filtration performance, while the antimicrobial activity is maintained even under dust-loaded conditions. To fabricate a highly permeable pre-filter, we employed 3D printing, which enables precise control over the fibre diameter and pore geometry at the sub-millimetre scale, allowing the construction of a large-fibre (~0.5 mm), open-mesh structure that minimises particulate deposition while maintaining high air permeability.

TPU pre-filters were fabricated using an FFF-based 3D printer. The extrusion nozzle and heated plate facilitated

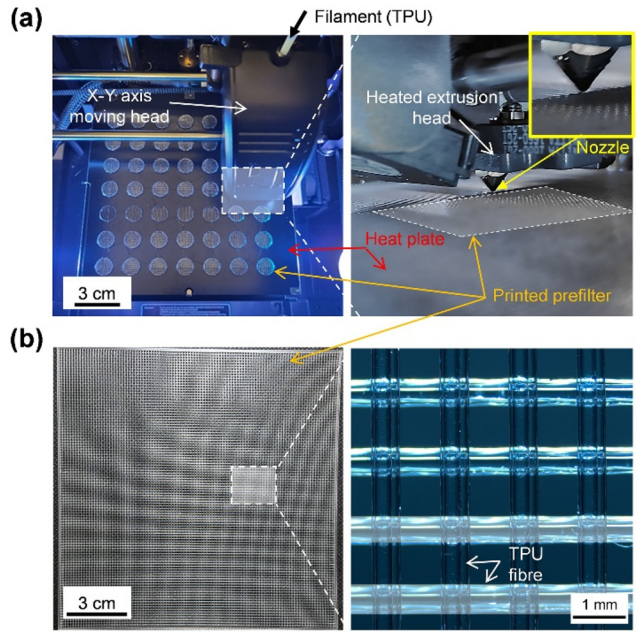

Fig. 1 (a) Photographs of the FFF-based 3D printing process, showing multiple TPU pre-filters. (b) Optical microscopy image and fibre diameter distribution of the 3D-printed TPU pre-filter, confirming a uniform fibre alignment and narrow size variation.

uniform deposition of TPU filaments through precise layer-by-layer stacking. As shown in Fig. 1a, multiple circular pre-filter discs were simultaneously printed on the heated plate. Fig. 1b presents a large-area square pre-filter (14 cm × 14 cm) fabricated at the maximum printable area of our 3D printer. This large filter retains the same mesh design (fibre diameter: 0.42 mm, spacing: 0.88 mm) as the 1.27 cm circular filter, and the fibres were highly aligned, free from distortion, and exhibited smooth surfaces with consistent spacing (Fig. S1c). Optical microscopy analysis revealed an average fibre diameter of 543.8 ± 3.3 μm with a narrow size distribution (Fig. S1d). These results demonstrate that 3D printing offers precise control over the fibre diameter, spacing, and thickness, enabling reproducible fabrication of structurally uniform pre-filters with consistent performance.

AuNCs were synthesised using a CO-directed reduction method.[24] Their size, composition, and optical features were analysed. As shown in Fig. 2a, the UV-Vis absorption spectrum of the AuNC solution exhibited distinct peaks at 400, 450, 670, and 780 nm, consistent with the reported absorption profiles of $[Au_{25}(Cys)_{18}]$ in previous studies.[26,27] To confirm AuNC composition, ESI-MS was performed (Fig. 2b and c). The most intense peak appeared at m/z 2361.46 (#1) within the range of m/z 1500–4000, accompanied by additional peaks (#2–6) corresponding to proton dissociation and sodium coordination of $[Au_{25}(Cys)_{18}]$. The isotope pattern of peak #1 displayed a 0.33 spacing between ^{12}C and ^{13}C (Fig. S4), confirm-

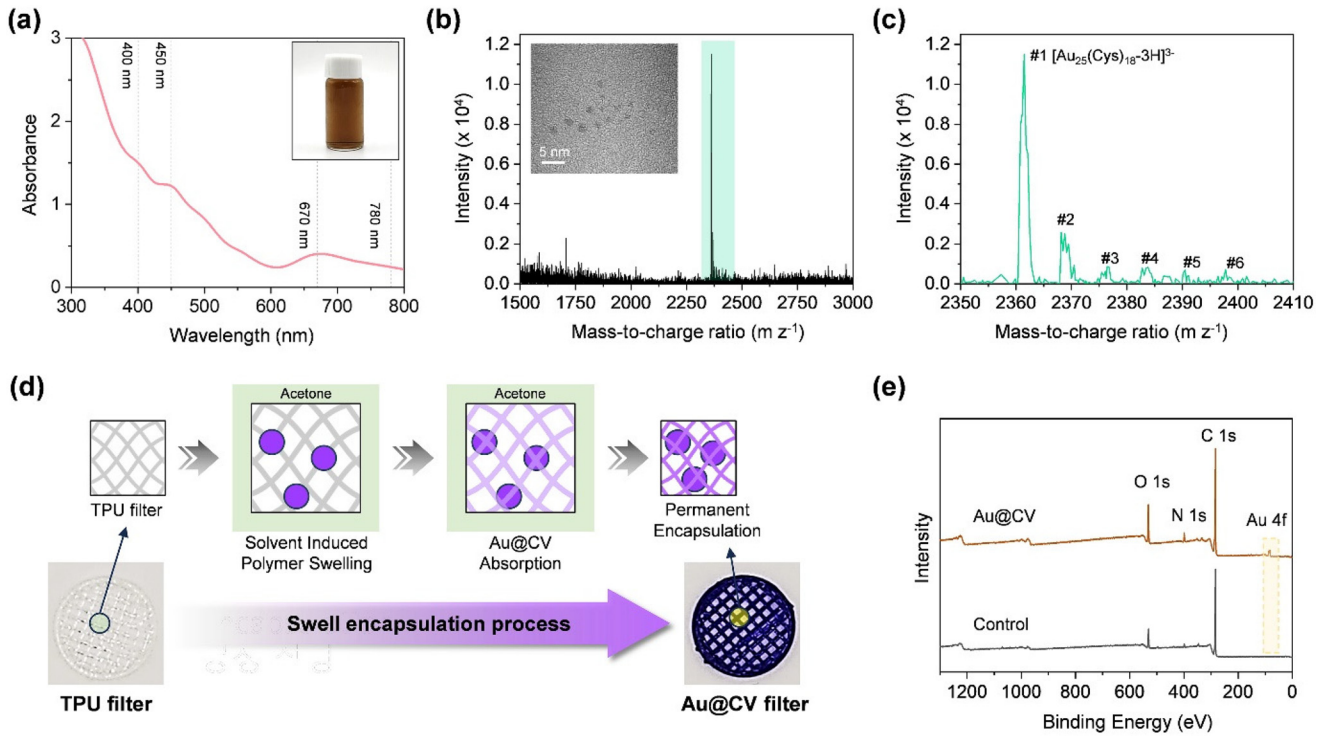

Fig. 2 (a) UV-Vis absorption spectrum of AuNCs ($[Au_{25}(Cys)_{18}]$). (b and c) Electrospray ionisation-mass spectra (ESI-MS) of AuNCs, with the inset showing the HRTEM image of AuNCs. (d) Schematic illustration of the swelling–shrinkage encapsulation process used to produce Au@CV-coated pre-filters (Au@CV filter). (e) XPS survey spectra of control, CV, and Au@CV filters.

ing the formation of $[Au_{25}(Cys)_{18}–3H^{+}]^{3-}$ ions under ESI conditions, with a molecular weight of 7084.38 Da. Other detected ion species were $[Au_{25}(Cys)_{18}–4H + Na]^{3-}$ (7104.39 Da), $[Au_{25}(Cys)_{18}–5H + 2Na]^{3-}$ (7128.36 Da), $[Au_{25}(Cys)_{18}–6H + 3Na]^{3-}$ (7148.28 Da), $[Au^{25}(Cys)^{18}–7H + 4Na]^{3-}$ (7171.38 Da), and $[Au_{25}(Cys)_{18}–8H + 5Na]^{3-}$ (7191.93 Da) (Table S1). Theoretical peak positions matched well with the experimental data, validating the successful synthesis of $[Au_{25}(Cys)_{18}]$.[26–28] High-resolution TEM confirmed an average AuNC size of below 2 nm (inset of Fig. 2b).

To functionalise the 3D-printed TPU pre-filter, CV and AuNCs were incorporated into the TPU filter *via* a swelling–encapsulation–shrinkage process (Fig. 2d).[29] In this process, the TPU filter was first swollen in acetone, allowing the dye molecules and AuNCs to diffuse into the polymer matrix. Upon solvent removal, the polymer shrank back to its original size, entrapping the CV molecules within the fibres. The treated pre-filter appears as a distinct purple colour due to the presence of CV, whereas AuNCs alone did not cause a visible colour change. The UV-Vis absorption spectrum of the CV-coated surface exhibited a main absorbance at ~600 nm with a shoulder peak at ~530 nm (Fig. S5). As the dipping time increased, the surface gradually began to exhibit a more pronounced purple colour, accompanied by a continuous increase in absorbance at 600 nm (Fig. S6). In the XPS overall survey of the Au@CV filters, Au 4f peaks (at 83.38 and 87.08 eV) and an enhanced N 1s peak (at 398.78 eV) were observed, confirming the successful incorporation of both CV and AuNCs into the filter (Fig. 2e and S7).

In the real world, the pre-filter surface is inevitably and continuously exposed to various forms of contact and wear. The Au@CV coating exhibited excellent mechanical stability, as confirmed by an adhesive tape-peeling test, where the absorbance at 600 nm remained nearly unchanged even after 150 peeling cycles (Fig. S8a). To assess operational stability, the robustness of the Au@CV filter was further tested under airflow conditions representative of real filtration systems. No evidence of surface detachment or structural degradation was observed during the test (Fig. S9). Furthermore, since the pre-filter may encounter moisture from humidity, breath, or rain, water stability was investigated by immersing the coated surface in DI water and periodically monitoring its absorbance at 600 nm. As shown in Fig. S8b and c, only negligible leaching (~0.6 ppm) of CV occurred after 24 h, with no additional leaching detected over 48 h. These results confirm that the swell–encapsulation coating provides a stable and durable immobilisation of Au@CV on TPU under mechanical or environmental stress.

Antibacterial performance

The antibacterial activity of the functionalised pre-filters was assessed against *S. epidermidis* under dark and illuminated conditions. As shown in Fig. 3a, neither CV nor Au@CV filters exhibited significant antibacterial activity in the dark (*t*-test, $p > 0.1$). Under visible-light irradiation, CV filters demonstrated a light-intensity-dependent effect, achieving log reductions of 0.3, 0.5, and 0.8 after 3 h at 0.04, 5.8, and 11.9 mW cm^{-2}, respectively. It has been reported that upon light irradiation, CV generates ROS that are lethal to bacteria, through both Type I (electron transfer to O_2/H_2O, producing $O_2^{\bullet-}$, H_2O_2 and $^{\bullet}OH$) and Type II (energy transfer to $^3O_2$, yielding $^1O_2$) pathways.[30,31] Our previous studies demonstrated that the antimicrobial activity of CV-coated surfaces was primarily attributed to $^1O_2$, indicating that CV itself predominantly produces $^1O_2$ *via* the Type II pathway.[30] The incorporation of AuNCs into CV filters significantly enhanced the antibacterial efficacy. Even after 1 h of irradiation, Au@CV filters achieved log reductions of 0.6, 1.2, and 1.3 at 0.04, 5.8, and 11.9 mW cm^{-2}, respectively (*t*-test, $p < 0.05$). After 3 h at >5.8 mW cm^{-2}, the Au@CV filter reached up to 4.7 log reduction in viable bacteria. This effect was observed for both Gram-positive (*S. epidermidis*) and Gram-negative (*E. coli*) bacteria. However, the latter exhibited lower inactivation because *E. coli* possesses more complex membrane structures (Fig. S10).[32,33,34–36] ROS scavenger/quencher assays were performed to identify the species responsible for the enhanced antibacterial activity (Fig. 3b). The antimicrobial performance was significantly suppressed after the addition of the H_2O_2 scavenger (from >4.4 to 2.8-log reduction) and the $^1O_2$ quencher (from >4.4 to 2.5-log reduction), whereas other scavengers showed negligible effects, indicating that AuNC incorporation enhanced H_2O_2 generation, which is related to a redox reaction. Thus, it is speculated that the simultaneous generation of multiple oxygen species produced a synergistic effect and/or multi-site attack on bacterial cells, leading to enhanced antibacterial performance.

To elucidate the enhancement mechanisms, steady-state PL spectra were measured (Fig. 3c). CV-coated samples exhibited strong PL intensity, reflecting recombination of photogenerated charge carriers, whereas Au alone showed no response. After AuNC incorporation into the CV-coated sample, PL intensity markedly decreased, indicating reduced charge carrier recombination. Time-resolved PL analysis confirmed shorter PL lifetimes for Au@CV compared to CV alone (Fig. 3d), suggesting charge carrier transfer from CV to AuNCs. To understand the mechanism of this transfer, band alignment between the materials was calculated using XPS data (Fig. 3e and S7b, S11). CV and AuNCs exhibited optical band gap energies of 1.91 eV and 1.03 eV, respectively, with HBM (E^{HBM}) values of 1.29 eV (CV) and 1.01 eV (AuNCs). Binding energy differences between the N 1s core level (CL) and E^{HBM} were investigated in CV alone, AuNCs alone, and Au@CV to determine the band alignment (Fig. S7b, S11c and f). The gaps between N 1s CL and E^{HBM} were 398.31 eV for CV alone and 398.19 eV for AuNCs alone, respectively, confirming that the E^{HBM} of CV was 0.12 eV higher than that of AuNCs. The lowest unoccupied molecular orbital (LUMO) band minimum (E^{LBM}) of CV was 0.12 eV higher than that of AuNCs, forming a Type I straddling band alignment. It is suggested that this alignment facilitates photoexcited electron transfer from the LUMO band of CV to the LUMO band of AuNCs, inducing surface redox reactions and enhancing H_2O_2 generation in the combination.[9,25]

The stability of antibacterial activity was evaluated under accelerated ageing at 11.9 mW cm^{-2} (Fig. 3f). The initial antimicrobial efficacy, corresponding to a 4.7 log reduction in viable

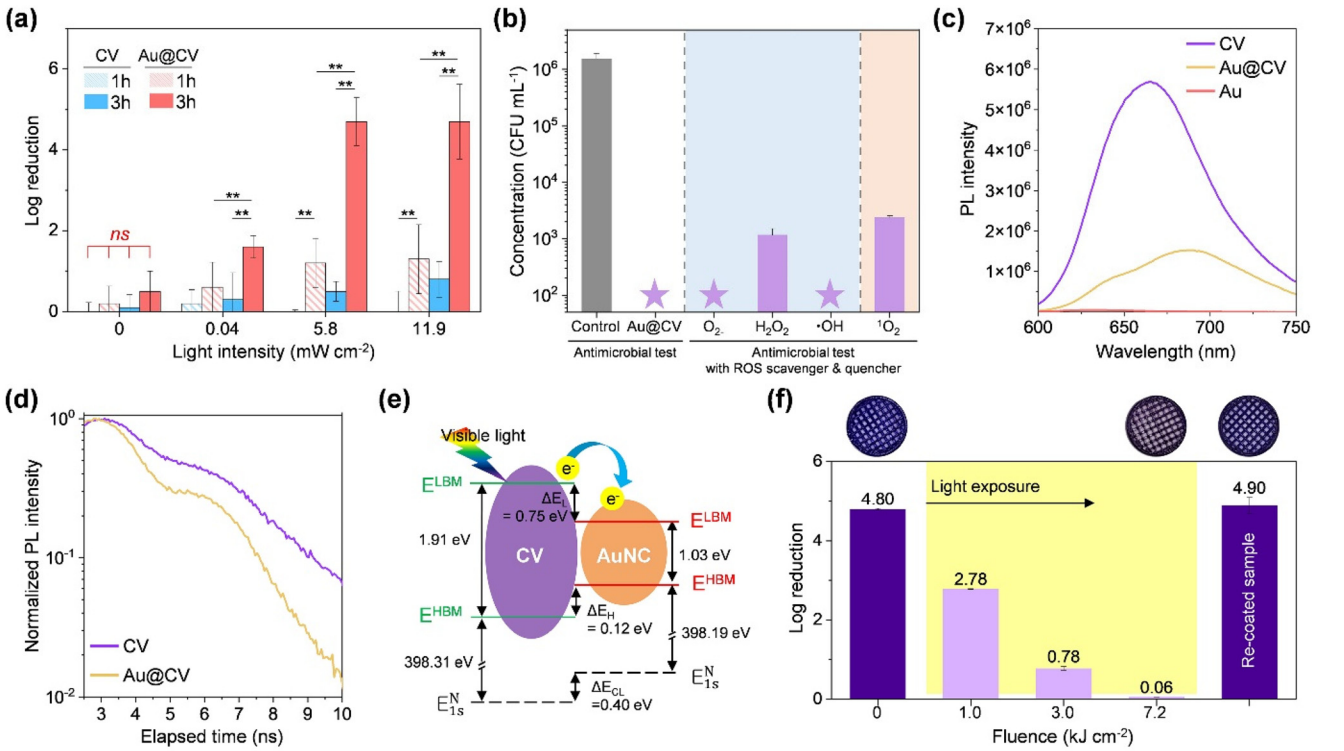

Fig. 3 (a) Antibacterial activity of CV- and Au@CV-coated pre-filters against *S. epidermidis* under different light intensities and exposure times. ** denotes $p < 0.01$. (b) Identification of the ROS responsible for the antimicrobial performance of the Au@CV pre-filter under visible light through scavenger/quencher assays. Stars represent values below the detection limit (<50 CFU mL^{-1}). (c) Steady-state PL spectra (λ_{ex} = 560 nm) of CV, Au, and Au@CV filters. (d) Time-resolved PL decay lifetime ($\lambda_{ex}/\lambda_{em}$ = 560/620 nm) for CV-only and Au@CV filters, (e) band alignment between CV and AuNCs determined from XPS and UV-Vis analyses. (f) Photostability of Au@CV filters under 11.9 mW cm^{-2} irradiation and recovery of photobactericidal activity *via* simple recoating.

bacteria, gradually declined with a prolonged exposure to visible light, in parallel with CV photobleaching. After a cumulative light dose of 3.0 kJ cm^{-2}, equivalent to 2.4 years of indoor light exposure (0.04 mW cm^{-2}), the antimicrobial efficacy decreased to ~0.8 log reduction. Nevertheless, this level of activity remained comparable to or stronger than that of CV alone under 11.9 mW cm^{-2}. Importantly, the antibacterial function was easily restored after 24 h immersion in CV solution, underscoring the recyclability and practical applicability of Au@CV filters.

Filter system performance evaluation

Fig. 4a presents the concept and performance of the antimicrobial filter system integrating an Au@CV pre-filter with a conventional main filter. The two filters play complementary roles: the Au@CV filter serves as an antimicrobial interface by generating ROS, while the main filter captures aerosols. When airborne *S. epidermidis* (peak diameter of ~576 nm) was introduced, the main filter achieved a fractional filtration efficiency of ~82%, whereas the Au@CV filter, due to its larger pore size, showed only ~11% efficiency (Fig. 4b). Importantly, integrating the Au@CV filter did not increase the pressure drop compared with the main filter alone (Fig. 4c), across surface velocities of 2.3–11.7 cm s^{-1}, covering the U.S. Department of Energy's standard airflow range.[37] To evaluate the effect of integrating the pre-filter on filtration performance, the quality factor (QF) was calculated using the following formula:[7]

$$\mathrm{QF} = -\ln(1 - \eta_{\mathrm{peak}})/\Delta P \quad (3)$$

where η_{peak} is the filtration efficiency at the peak diameter of *S. epidermidis*. The QF values for the main filter, the Au@CV pre-filter, and the combined filter system were 0.11, 0.04, and 0.10 Pa^{-1}, respectively. These results indicate that integrating the Au@CV pre-filter does not compromise the filtration performance of the main filter, supporting our strategy of incorporating a visible-light-activated antimicrobial pre-filter without introducing a pressure-drop penalty.

Upon visible-light irradiation, the Au@CV pre-filter produced ROS that contributed to two distinct antimicrobial pathways: (i) direct photochemical inactivation, where ROS inactivate microbes deposited on the Au@CV surface independently of airflow, and (ii) airflow-assisted inactivation, where ROS are transported downstream and act upon microbes trapped on the main filter (Fig. 4a). As shown in Fig. 4d, the antibacterial activity of the Au@CV filter remained stable regardless of flow conditions, consistent with a direct ROS–microbe contact mechanism. In contrast, the main filter exhibited strong airflow dependence, reaching ~98% antibacterial efficiency under normal flow, which increased to 99.2% at higher vel-

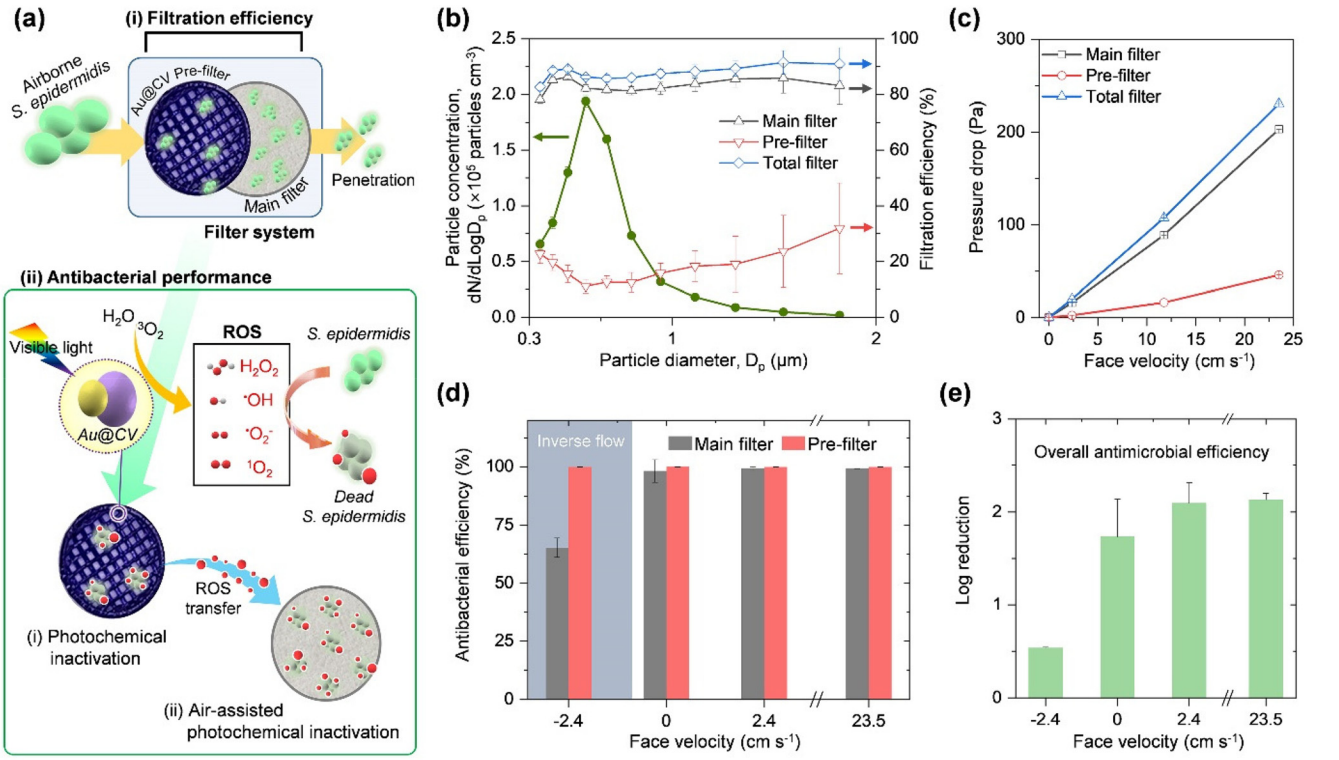

Fig. 4 (a) Conceptual design of the integrated filter system combining an Au@CV pre-filter with a downstream main filter, highlighting direct and airflow-assisted ROS-mediated inactivation. (b) Particle size distribution of airborne *S. epidermidis* (green line) and fractional filtration efficiencies of the Au@CV and main filters. (c) Pressure drop across the tested filters under varying face velocities. (d) Comparison of the antibacterial activity between Au@CV and main filters, showing contributions of direct and airflow-assisted effects. (e) Overall antibacterial efficiency of the integrated system expressed as log reduction under different flow conditions.

ocities due to enhanced ROS transfer. When the flow direction was reversed, the antibacterial efficiency of the main filter dropped to ~65%, confirming that ROS are transported downstream *via* airflow. The partial retention of activity under reversed flow further indicates that diffusion also contributes to ROS delivery.[8,38] The lifetime of singlet oxygen in the air under atmospheric conditions (23 °C and 1 atm) has been reported as 2.80 s, which enables the antimicrobial effects up to 0.6–0.8 cm.[39] The overall antibacterial efficiency quantified by log reduction is presented in Fig. 4e. Without airflow, the system achieved a log reduction of 1.73, which increased to 2.1 under a face velocity of 2.4 cm s^{-1}. Under reversed flow, however, the log reduction decreased to 0.53. In addition, it was confirmed that airflow-assisted ROS inactivation did not affect the filtration efficiency of the main filter. This might be because H_2O_2 and $^1O_2$, which are neutral molecules, did not adversely affect the electrostatic charge or the fibre structure of the main filter (Fig. S12).

4. Conclusion

We developed a reusable antimicrobial filter system by functionalising a 3D-printed TPU pre-filter with CV and AuNCs. The resulting Au@CV filter exhibited strong visible-light-driven antibacterial activity against *S. epidermidis*, achieving a 4.7 log reduction in viable bacteria. This effect was attributed to the promotion of charge-carrier transfer between CV and AuNCs, leading to ROS generation under visible light. ROS scavenger and quenching assays confirmed that H_2O_2 and $^1O_2$ were the primary contributors to the enhanced antimicrobial performance. In addition, the filter's activity could be readily restored through a simple re-dyeing process. When integrated with a conventional main filter, the system maintained a negligible pressure drop across operational airflow ranges, ensuring high air permeability. Importantly, the Au@CV filter acted as a source of ROS that diffused downstream, enabling >99% antibacterial efficiency in the untreated main filter. It is expected that this reusable, cost-effective, and scalable strategy could be readily integrated into existing air filtration systems to prevent the spread of infectious bioaerosols in hospitals, offices, and public places.

Conflicts of interest

The authors declare no competing financial interests.

Data availability

Raw data supporting the figure graphs in the research paper are available at figshare at **https://doi.org/10.6084/m9.figshare.30256420**.

Supplementary information (SI) is available. Raw data for all graphs presented in the article and in the supplementary information have been provided. See DOI: https://doi.org/10.1039/d5qi02008e.

Acknowledgements

This work was supported by the National Research Foundation of Korea (NRF) grant funded by the Korea Government (MSIT) (RS-2023-00213266; RS-2024-00446841).

References

1 J. Douwes, P. Thorne, N. Pearce and D. Heederik, Bioaerosol health effects and exposure assessment: progress and prospects, *Ann. Occup. Hyg.*, 2003, **47**, 187–200.
2 K.-H. Kim, E. Kabir and S. A. Jahan, Airborne bioaerosols and their impact on human health, *J. Environ. Sci.*, 2018, **67**, 23–35.
3 S. Gautam and U. Trivedi, Global implications of bioaerosol in pandemic, *Environ. Dev. Sustain.*, 2020, **22**, 3861–3865.
4 I. Lee, K. S. Kim, D. Y. Lee and J. Lee, Hierarchical three-layered fibers for bioaerosol and CO_2 capture, and antimicrobial performance, *Appl. Surf. Sci.*, 2024, **670**, 160623.
5 I. Lee, K. S. Kim, J. Lee, G. M. Kim, J. H. Jung and D. Y. Choi, Curled silica nanostructures formed on filter membranes for efficient bioaerosol and particulate matter removal, *Appl. Surf. Sci.*, 2024, **661**, 160026.
6 D. U. Lee, S. B. Jeong, B. J. Lee, S. K. Park, H. M. Kim, J. H. Shin, S. Y. Lee, G. Kim, J. Park, G. M. Kim, J. H. Jung and D. Y. Choi, Antimicrobial and antifouling effects of petal–like nanostructure by evaporation–induced self–assembly for personal protective equipment, *Small*, 2024, **20**, 2306324.
7 K. J. Heo, S. B. Jeong, J. Shin, G. B. Hwang, H. S. Ko, Y. Kim, D. Y. Choi and J. H. Jung, Water-repellent TiO_2-organic dye-based air filters for efficient visible-light-activated photochemical inactivation against bioaerosols, *Nano Lett.*, 2021, **21**, 1576–1583.
8 S. B. Jeong, D. U. Lee, B. J. Lee, K. J. Heo, D. W. Kim, G. B. Hwang, A. J. MacRobert, J. H. Shin, H. S. Ko, S. K. Park, Y. S. Oh, S. J. Kim, D. Y. Lee, S. -B. Lee, I. Park, S. B. Kim, B. Han, J. H. Jung and D. Y. Choi, Photobiocidal-triboelectric nanolayer coating of photosensitizer/silica-alumina for reusable and visible-light-driven antibacterial/antiviral air filters, *Chem. Eng. J.*, 2022, **440**, 135830.
9 S. Y. Lee, J. H. Shin, I. H. Kim, D. Y. Choi, D. U. Lee, G. B. Hwang, B. Han, S. B. Kim, D.-K. Song, I. Park and J. H. Jung, Transparent and visible light-activated antimicrobial air filters from electrospun crystal violet-embedded polyacrylonitrile nanofibers, *Environ. Res.*, 2025, **266**, 120490.
10 S. K. Park, S. Y. Lee, S. B. Kim, I. H. Kim, D. U. Lee, J. H. Shin, J. S. Son, G. Kim, S. H. Yoo, D. Y. Lee, J. H. Jung and D. Y. Choi, Dual–action antibacterial nanoblades for rapid inactivation of bioaerosols in personal protective equipment, *Adv. Funct. Mater.*, 2025, **35**, 2421728.
11 K. S. Kim, I. Lee and J. Lee, Synergetic chemo-mechano antimicrobial puncturable nanostructures for efficient bioaerosol removal, *BioChip J.*, 2024, **18**, 439–452.
12 W. Liu, Y. Sun, A. Cui, Y. Xia, Q. Yan, Y. Song, L. Wang, G. Shan and X. Wang, Electrothermal sterilization and self-powered real-time respiratory monitoring of reusable mask based on Ag micro-mesh films, *Nano Energy*, 2023, **105**, 107987.
13 S. Han, J. Kim, Y. Lee, J. Bang, C. G. Kim, J. Choi, J. Min, I. Ha, Y. Yoon and C.-H. Yun, Transparent air filters with active thermal sterilization, *Nano Lett.*, 2022, **22**, 524–532.
14 Y. H. Joe, W. Ju, J. H. Park, Y. H. Yoon and J. Hwang, Correlation between the antibacterial ability of silver nanoparticle coated air filters and the dust loading, *Aerosol Air Qual. Res.*, 2013, **13**, 1009–1018.
15 K. Majchrzycka, M. Okrasa, A. Jachowicz, J. Szulc and B. Gutarowska, Microbial growth on dust-loaded filtering materials used for the protection of respiratory tract as a factor affecting filtration efficiency, *Int. J. Environ. Res. Public Health*, 2018, **15**, 1902.
16 K. Majchrzycka, M. Okrasa, J. Szulc and B. Gutarowska, The impact of dust in filter materials of respiratory protective devices on the microorganisms viability, *Int. J. Ind. Ergon.*, 2017, **58**, 109–116.
17 N. G. Reed, The history of ultraviolet germicidal irradiation for air disinfection, *Public Health Rep.*, 2010, **125**, 15–27.
18 D.-K. Kim and D.-H. Kang, UVC LED irradiation effectively inactivates aerosolized viruses, bacteria, and fungi in a chamber-type air disinfection system, *Appl. Environ. Microbiol.*, 2018, **84**, e00944–e00918.
19 M. Yamamoto, M. Nishioka and M. Sadakata, Sterilization by H_2O_2 droplets under corona discharge, *J. Electrost.*, 2002, **55**, 173–187.
20 T. Xia and C. Chen, Evolution of pressure drop across electrospun nanofiber filters clogged by solid particles and its influence on indoor particulate air pollution control, *J. Hazard. Mater.*, 2021, **402**, 123479.
21 Y. Zhou, Y. Liu, M. Zhang, Z. Feng, D.-G. Yu and K. Wang, Electrospun nanofiber membranes for air filtration: A review, *Nanomaterials*, 2022, **12**, 1077.
22 M. Zhu, J. Han, F. Wang, W. Shao, R. Xiong, Q. Zhang, H. Pan, Y. Yang, S. K. Samal and F. Zhang, Electrospun nanofibers membranes for effective air filtration, *Macromol. Mater. Eng.*, 2017, **302**, 1600353.
23 X. Xu, S. Xiao, H. J. Willy, T. Xiong, R. Borayek, W. Chen, D. Zhang and J. Ding, 3D-printed grids with polymeric photocatalytic system as flexible air filter, *Appl. Catal., B*, 2020, **262**, 118307.
24 Y. Yu, Z. Luo, Y. Yu, J. Y. Lee and J. Xie, Observation of cluster size growth in CO-directed synthesis of $Au_{25}(SR)_{18}$ nanoclusters, *ACS Nano*, 2012, **6**, 7920–7927.

25 G. B. Hwang, H. Huang, G. Wu, J. Shin, A. Kafizas, K. Karu, H. D. Toit, A. M. Alotaibi, L. Mohammad-Hadi, E. Allan, A. J. MacRobert, A. Gavriilidis and I. P. Parkin, Photobactericidal activity activated by thiolated gold nanoclusters at low flux levels of white light, *Nat. Commun.*, 2020, **11**, 1207.

26 H. Huang, G. B. Hwang, G. Wu, K. Karu, H. Du Toit, H. Wu, J. Callison, I. P. Parkin and A. Gavriilidis, Rapid synthesis of $[Au_{25}(Cys)_{18}]$ nanoclusters via carbon monoxide in microfluidic liquid-liquid segmented flow system and their antimicrobial performance, *Chem. Eng. J.*, 2020, **383**, 123176.

27 G. B. Hwang, G. Wu, J. Shin, L. Panariello, V. Sebastian, K. Karu, E. Allan, A. Gavriilidis and I. P. Parkin, Continuous single-phase synthesis of $[Au_{25}(Cys)_{18}]$ nanoclusters and their photobactericidal enhancement, *ACS Appl. Mater. Interfaces*, 2020, **12**, 49021–49029.

28 G. B. Hwang, K. J. Heo, W. Jee, L. Panariello, J. Piovesan, M. Cornwell, A. Collauto, A. Kafizas, S. Ali, C. Knapp, A. J. MacRobert, A. Gavriilidis, I. P Parkin, S. M. Woodley and J. H. Jung, Optimizing the Au particle doping size for enhanced photocatalytic disinfection under low-intensity visible light, *ACS Nano*, 2025, **19**, 27740–27753.

29 C. R. Crick, S. Noimark, W. J. Peveler, J. C. Bear, A. P. Ivanov, J. B. Edel and I. P. Parkin, Advanced analysis of nanoparticle composites–a means toward increasing the efficiency of functional materials, *RSC Adv.*, 2015, **5**, 53789–53795.

30 K. J. Heo, D. U. Lee, J. H. Shin, J. Park, B. J. Lee, J. Shin, S. B. Jeong, G. B. Hwang, A. J. MacRobert, I. P. Parkin, J. H. Jung and D. Y. Choi, Transparent, robust, and photochemical antibacterial surface based on hydrogen bonding between a Si-Al and cationic dye, *ACS Appl. Mater. Interfaces*, 2022, **14**, 53285–53297.

31 S. J. Beech, S. Noimark, K. Page, N. Noor, E. Allan and I. P. Parkin, Incorporation of crystal violet, methylene blue and safranin O into a copolymer emulsion; the development of a novel antimicrobial paint, *RSC Adv.*, 2015, **5**, 26364–26375.

32 B. U. Lee, S. H. Yun, J. H. Jung and G.-N. Bae, Effect of relative humidity and variation of particle number size distribution on the inactivation effectiveness of airborne silver nanoparticles against bacteria bioaerosols deposited on a filter, *J. Aerosol Sci.*, 2010, **41**, 447–456.

33 D. Y. Choi, K. J. Heo, J. Kang, E. J. An, S.-H. Jung, B. U. Lee, H. M. Lee and J. H. Jung, Washable antimicrobial polyester/aluminum air filter with a high capture efficiency and low pressure drop, *J. Hazard. Mater.*, 2018, **351**, 29–37.

34 X. Liang, M. Sun, L. Li, R. Qiao, K. Chen, Q. Xiao and F. Xu, Preparation and antibacterial activities of polyaniline/$Cu_{0.05}Zn_{0.95}O$ nanocomposites, *Dalton Trans.*, 2012, **41**, 2804–2811.

35 A. Azam, A. S. Ahmed, M. Oves, M. S. Khan and A. Memic, Size-dependent antimicrobial properties of CuO nanoparticles against Gram-positive and -negative bacterial strains, *Int. J. Nanomed.*, 2012, **7**, 3527–3535.

36 J. H. Shin, S. B. Jeong, I. H. Kim, S. Y. Lee, G. B. Hwang, I. Park, K. J. Heo and J. H. Jung, Performance comparison of photodynamic antimicrobial chemotherapy with visible-light-activated organic dyes: Rose bengal, crystal violet, methylene blue, and toluidine blue O, *Environ. Res.*, 2023, **238**, 117159.

37 U.S. Department of Energy: *Specification for HEPA Filters Used by DOE Contractors*, DOE-STD-3020-97, U.S. Department of Energy, Washington, D.C., 1997.

38 H. Shen, Z. Zhou, H. Wang, J. Chen, M. Zhang, M. Han, Y. Shen and D. Shuai, Photosensitized electrospun nanofibrous filters for capturing and killing airborne coronaviruses under visible light irradiation, *Environ. Sci. Technol.*, 2022, **56**, 4295–4304.

39 K.-K. Wang, S. Song, S.-J. Jung, J.-W. Hwang, M.-G. Kim, J.-H. Kim, J. Sung, J.-K. Lee and Y.-R. Kim, Lifetime and diffusion distance of singlet oxygen in air under everyday atmospheric conditions, *Phys. Chem. Chem. Phys.*, 2020, **22**, 21664–21671.